Talanta 226 (2021) 122165

Contents lists available at ScienceDirect

Talanta

journal homepage: www.elsevier.com/locate/talanta

# Electrochemical sensor based on magnetic nanohybrids of multiple phthalocyanine doped ferrites/CMWCNTs for detection of rosmarinic acid

Zihua Wang, Yunyun Wang, Shengnan Yang, Lan Xue, Wei Feng, Xinran Liu, Binshuai Li, Mengai Yin, Jun Jiao **, Qiang Chen *

*The Key Laboratory of Bioactive Materials Ministry of Education, College of Life Science, Nankai University, Weijin Road No.94, Tianjin, 300071, PR China*

ARTICLE INFO

*Keywords:*
$Fe_3O_4$
$ZnFe_2O_4$
Phthalocyanine
CMWCNTs
Hybrid ferrites
Rosmarinic acid

ABSTRACT

Ferrites have attracted considerable attention in biosensor developments owing to their favorable electrochemical and magnetic properties. Speedy and trace analysis can be succeeded by the sensors based on magnetic nanohybrids. In this work, we reported a novel method for one-step synthesis of magnetic ferrites composed of Fe and phthalocyanine. After hybridization with carbonylated multi wall carbon nanotubes, a sensor based on $Fe_3O_4$-Pc-CMWCNTs nanocomposites was fabricated for the detection of rosmarinic acid (RA), a bioactive phytochemical. The sensor can be constructed within 30s without any complicated process. A comparison of electrochemical activity between $ZnFe_2O_4$-Pc-CMWCNTs and $Fe_3O_4$-Pc-CMWCNTs nanohybrids also has been accomplished in this work. Compared with $ZnFe_2O_4$-Pc-CMWCNTs based on commonly used ferrites, $Fe_3O_4$-Pc-CMWCNTs/MGCE exhibited a higher catalytical ability for the detection of RA. The sensor modified with $Fe_3O_4$-Pc-CMWCNTs displayed a low LOD of 0.182 μM with a wide linear range from 0.2 to 400 μM, which was 30 times more sensitive than the one based on $ZnFe_2O_4$-Pc-CMWCNTs. The obtained sensor also owned an excellent selectivity, reproducibility, repeatability, and stability, which made it achieve the measurements in plant sample and human serum.

## 1. Introduction

Rosmarinic acid (RA) as a bioactive phytochemical endows notable pharmacological activities, which can combat several diseases like cancer [1,2], diabetes [3], and cardiovascular diseases [4,5]. It has the capacity to defend the attacks of virus [6], reactive oxygen species [7,8], and inflammation [9,10], revealing a great potential to be a therapeutic drug. As a natural compound, it is difficult to partition and assess RA in a complex system because of the interferential phenomena, which sets a strict requirement for the analytic methods of RA. Compared to the existed approaches, like HPLC-ELSD [11], UV–vis spectrophotometry [12], and ultra-fast liquid chromatography (UFLC) [13], the sensitivity and simplicity of biosensors allow them to be used in where lacks sophisticated operators with speedy processes [14,15]. It is worth mentioning that the selectivity of biosensors makes them applicable to implement the trace RA test [16]. Therefore, developing rapid strategies for the sensor construction and enhancing the detective ability are of great significance for the analysis of RA.

Spinel-type ferrites are the metal oxides with ferrimagnetic features composed of iron elements as the main ingredient with a general formula of $MFe_2O_4$, where M stands for transition metals like Mn, Fe, Co, Ni, Cu, and Zn [17,18]. They have become ideal candidates for the construction of biosensor on the grounds that the nanomaterials can be separated from the reaction solution by an external magnet without complicated filtration and centrifugation steps [19]. In spite of the magnetic properties, they are also outstanding catalysts [20,21]. Especially, magnetite and Zn-doped ferrite have been widely used in photocatalysis and sensing due to their favorable stability and good magnetic property [22,23]. For example, Hassan Karimi-Maleh et al. reported an electrochemical sensor using a nano $Fe_3O_4$ ionic liquid paste electrode to simultaneously detect two water contaminants, namely 2-phenylphenol and 4-chlorophenol. Due to the high catalytic ability of $Fe_3O_4$ nanoparticles, the sensor accomplished the real test in orange rind and water samples with the admirable performance [24]. Meanwhile, ferrites are also recyclable after modification of the sensing surface with intact catalytic ability, making the analysis sustainable and eco-friendly

** Corresponding author.
* Corresponding author.
*E-mail addresses:* junjiao@nankai.edu.cn (J. Jiao), qiangchen@nankai.edu.cn (Q. Chen).

https://doi.org/10.1016/j.talanta.2021.122165
Received 20 November 2020; Received in revised form 23 January 2021; Accepted 27 January 2021
Available online 2 February 2021

[25,26]. However, aggregation and poor processability of ferrites will decrease their catalytic abilities, which limit the further applications in electrochemical sensors [27].

The incorporation of other nanomaterials and ferrites into nanohybrids can surmount the above obstacles. Phthalocyanine (Pc) is an organic substance with four isoindole units connected by nitrogen atoms [28,29]. It has an 18 π-electron aromatic macrocyclic structure, which will form an N–Fe–N inner structure with iron, accelerating the redox reaction as a result of the increased catalytic activity [30–32]. For instance, Zeng et al. used the high catalytic ability of iron (II) phthalocyanines for the functionalization of ZIF-8 in order to enhance the sensing performance towards trichloroacetic acid [33]. In particular, the expanded macrocycle structure of Pc will promote the electron migration among different parts of nanocomposites, which contribute to improving the conductivity of the nanohybrids [34]. Moreover, owing to the large surface and versatility for modifications, multiple walled carbon nanotubes have been employed as scaffolding materials for building up electrochemical sensors in recent years [35]. Some drawbacks of ferrites, such as the tendency to aggregate, can also be overcome with the assistance of carboxylated MWCNTs networks since they provide a large framework for loading ferrites with various types of modification [36]. CMWCNTs not only boost the solubility of the obtained materials but also provide more binding sites for modification to form stable complexes [37].

In this work, we report a one-pot protocol for green synthesis of magnetic $Fe_3O_4$-Pc nanoparticles using phthalonitrile and $FeCl_3$. After the carboxylation of MWCNTs, the $Fe_3O_4$-Pc NPs were loaded on the CMWCNTs networks via electrostatic adsorption to compose $Fe_3O_4$-Pc-CMWCNTs nanocomposites. Instead of time-consuming and complex modification of electrode, the sensing surface was well prepared within 30s through the strong attraction between $Fe_3O_4$-Pc-CMWCNTs and magnetic electrode for detection of rosmarinic acid. Additionally, we assembled $ZnFe_2O_4$-Pc-CMWCNTs/MGCE based on widely applied zinc ferrite as the counterpart to compare the electrochemical properties and analytical abilities of the sensors. $Fe_3O_4$-Pc-CMWCNTs nanocomposites displayed a higher conductivity and catalytic ability than the $ZnFe_2O_4$-Pc-CMWCNTs.

## 2. Experimental

### 2.1. Reagents and equipment

Iron (III) chloride hexahydrate ($FeCl_3{\cdot}6H_2O$), zinc chloride ($ZnCl_2$), ethylene glycol, 1,2-dicyanobenzene, polyethylene glycol (MW = 1000), sodium acetate (NaAc), absolute ethyl alcohol, rosmarinic acid (RA), potassium chloride (KCl), manganese chloride ($MnCl_2$), cupric nitrate ($CuNO_3$), nickel nitrate ($NiNO_3$), puerarin, chicoric acid, protocatechualdehyde, caffeic acid, gallic acid, pyrocatechol, luteolin, adrenaline, dopamine, and noradrenaline were full obtained from Sigma-Aldrich Inc. (Shanghai, China). MWCNTs (30–50 nm) was obtained from Chinese Academy of Sciences, the Institute of Organic Chemistry (Chengdu, China). Vitamin C (VC), Vitamin $B_2$ ($VB_2$) and Vitamin $B_6$ ($VB_6$) were obtained from Shanghai yuanye Bio-Technology Co. All chemicals were analytically pure and directly used in the experiments. And double distilled water was used throughout the analysis.

Fourier transform infrared spectroscopy (FTIR) was recorded using a Bruker Tensor (Germany). X-ray diffraction (XRD) was examined by Rigaku with Cu Kα radiation (Japan) for element analysis. Transmission electron microscope (TEM), and vibrating sample magnetometer (VSM) were applied by JEM 2100 (Japan Electron Optics Laboratory), PPMS-9 (Quantum Design, America), and EscaLab 250Xi (Thermo Fisher Scientific, America). With a typical three-electrode system, the cyclic voltammetry (CV), electrochemical impedance spectroscopy (EIS) and differential pulse voltammetry (DPV) were carried out by using electrochemical analyzer (CHI 760E, China) with software.

### 2.2. Synthesis of $Fe_3O_4$-Pc-CMWCNTs and $ZnFe_2O_4$-Pc-CMWCNTs

The hybrid ferrites-nanosphere $Fe_3O_4$-Pc was synthesized by a one-pot method using $FeCl_3{\cdot}6H_2O$ and phthalonitrile. Firstly, 3.375 g $FeCl_3{\cdot}6H_2O$, 9 g NaAc, 2.5 g polyethylene, and 0.75 g 1,2-dicyanobenzene were added into 100 ml ethylene glycol under magnetic stirring, and the mixture was ultrasonicated for 1 h. Then, the yellow-brown solution was transferred into autoclave for a solvent-thermal reaction at 200 °C for 15 h. The products were collected by centrifugation and washed with absolute ethyl alcohol and double distilled water at 8000 rpm for 5 min. The final sediment was re-dispersed in 330 ml double distilled water and denoted as $Fe_3O_4$-Pc. In this method, the $FeCl_3{\cdot}6H_2O$ was used as the template to form the metal phthalocyanine through the cyclotetramerization of 1,2-dicyanobenzene. Meanwhile, NaAc and the polyethylene assist in the formation of $Fe_3O_4$ and prevention of adhesion [38], respectively.

As for the preparation of CMWCNTs, after traditionally mixed acid treatment of MWCNTs, the solution was washed by double distilled water until the pH near to neutral. The CMWCNTs were dried in the oven at 90 °C for 24 h and collected for the formation of $Fe_3O_4$-Pc-CMWCNTs nanocomposites. After ultrasonication of $Fe_3O_4$-Pc nanosphere and CMWCNTs for 4 h, a magnet was used to remove the unconnected materials. To end, the final product was washed three times and resuspended in 10 mL double distilled water. To contrast the electrochemical property of different ferrites, we also synthesized the $ZnFe_2O_4$-Pc-CMWCNTs nanocomposites. Apart from the additional reagent $ZnCl_2$, the synthesis process of $ZnFe_2O_4$-Pc-CMWCNTs was as same as the $Fe_3O_4$-Pc-CMWCNTs.

### 2.3. Preparation of $Fe_3O_4$-Pc-CMWCNTs/MGCE

After polishing with 0.05 μm and 0.1 μm $Al_2O_3$ powders until getting a glass surface, the magnetic glassy carbon electrode (MGCE, including an easily remove magnet, $d = 5$ mm) was washed under ultrasonication with 20 mL absolute ethyl alcohol and deionized water. Based on the property of $Fe_3O_4$-Pc-CMWCNTs nanohybrids, the sensing surface can be prepared and reused easily. Before the electrochemical test, the $Fe_3O_4$-Pc-CMWCNTs nanocomposites was decorated on the MGCE surface within 30s via magnetic adsorption. When the experiment completed, the nanomaterials can be recollected by removing the internal magnet of the MGCE for further use (seen in Scheme 1).

### 2.4. The electrochemical experimental procedures

Cyclic voltammograms (CVs) experiments were performed form 0 V to 0.7 V with 0.05 V/s. Differential pulse voltammetry (DPV) were used 0.15 V–0.8 V with scan rate of 0.05 V/s. Britton-Robinson buffer (BR buffer) as supporting electrolyte dissolved RA for electrochemical test. The selectivity of the electrode $Fe_3O_4$-Pc-CMWCNTs/MGCE were evaluated in certain concentration of RA including several different types of interfering species such as vitamins ($VB_2$, $VB_6$, VC), and cations ($K^+$, $Mn^{2+}$, $Zn^{2+}$, $Cu^{2+}$, $Ni^{2+}$), and RA analogs (chicoric acid, protocatechualdehyde, puerarin), and phenolic Acid (caffeic acid, gallic acid, pyrocatechol, luteolin), and electroactive substances (adrenaline, dopamine, noradrenaline). Eight separately magnetic sensors were used for analysis in reproducibility test and one electrode for five continuous measured in 0.5 mM RA solution for repeatability test. The stability of the prepared sensor was stored at 4 °C in the refrigerator for 30 days, and investigated with an interval of five days in 0.6 mM standard RA solution.

For practical samples analysis, *salvia miltiorrhiza* roots and *perilla caulis* (buy from the local pharmacy) were mixed with 10 ml double distilled water and bath under 25 °C for 2 h, then the suspensions sieved through membrane to remove suspended substances. Clear supernatant liquid was obtained and stored in 4 °C refrigerator for farther analysis. Leach liquor and human serum samples were diluted to 10% by BR

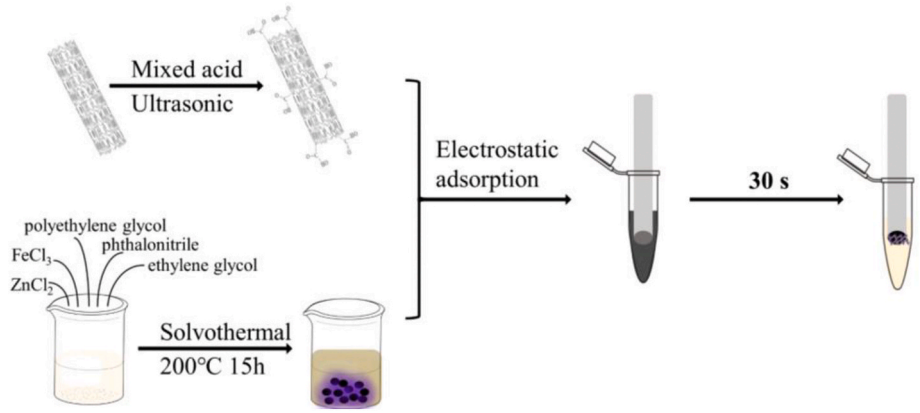


**Scheme 1.** The fabrication process of magnetic sensor.

buffer. All the appropriate amounts of RA were added using the standard addition method.

## 3. Results and discussion

### 3.1. Structure characterization of different composites

To verify the morphology, TEM was conducive to characterize the microstructure and internal crystal arrangement of the obtained materials. As shown in Fig. 1, the pristine $Fe_3O_4$ nanoparticles (Fig. 1A) exhibited a well-defined sphere structure with an average size of 80 nm, while the $Fe_3O_4$-Pc (Fig. 1B) had an irregular sphere surface in the size around 30 nm. In Fig. 1E, it can be obviously seen that $ZnFe_2O_4$ were spherical particles (about 100 nm) with rough appearances. With the addition of Pc, $ZnFe_2O_4$-Pc NPs presented a flower-like structure with concave cracks in an average diameter of 50 nm. Fig. S1 also demonstrated that the hybrid ferrites with the introduction of Pc had a smaller size with irregular structure than the ones without Pc, indicating the Pc not only attached to the surface of $Fe_3O_4$ and $ZnFe_2O_4$ but also inserted into the interior affecting the growth of magnetic nanohybrids [39,40]. Meanwhile, the TEM images of $Fe_3O_4$-Pc-CMWCNTs and $ZnFe_2O_4$-Pc-CMWCNTs nanocomposites are displayed in Fig. 1C and G. Apparently, $Fe_3O_4$-Pc NPs and $ZnFe_2O_4$-Pc NPs were anchored on the entangled CMWCNTs network, respectively. Fig.S1 C and F also proved that the obtained magnetic nanoparticles were distributed along the CMWCNTs, suggesting that the $Fe_3O_4$-Pc-CMWCNTs and $ZnFe_2O_4$-Pc-CMWCNTs nanocomposites had been composed successfully. $Fe_3O_4$-Pc-CMWCNTs (Fig. 1D) displays a shorter lattice length than $ZnFe_2O_4$-Pc-CMWCNTs (Fig. 1H), indicating a shorter interplanar distance for $Fe^{3+}$-$Fe^{2+}$hopping.

Vibrating sample magnetometer (VSM) is a typical means to explore the static magnetization of magnetic nanomaterials. As shown in Fig. 2A, $Fe_3O_4$ exhibited a high value of saturation magnetization (Ms) because $Fe^{2+}$ occupied B sites of the ferrites. Compared with $Fe_3O_4$-CMWCNTs, $Fe_3O_4$-Pc-CMWCNTs exhibited a lower magnetic moment which was caused by the decreases in unit weight of $Fe_3O_4$, implying the Pc had been introduced into $Fe_3O_4$-CMWCNTs.The same results could be observed in Zn-ferrites. In addition, $ZnFe_2O_4$-Pc-CMWCNTs had a smaller value of Ms than $Fe_3O_4$-Pc-CMWCNTs along with the adulteration of $Zn^{2+}$ since the increasing amount of $Zn^{2+}$ replaced $Fe^{2+}$on the B sites. Even though the induction of Pc diminished the magnetic moment of nanohybrids, the speedy modification of the sensing surface has not

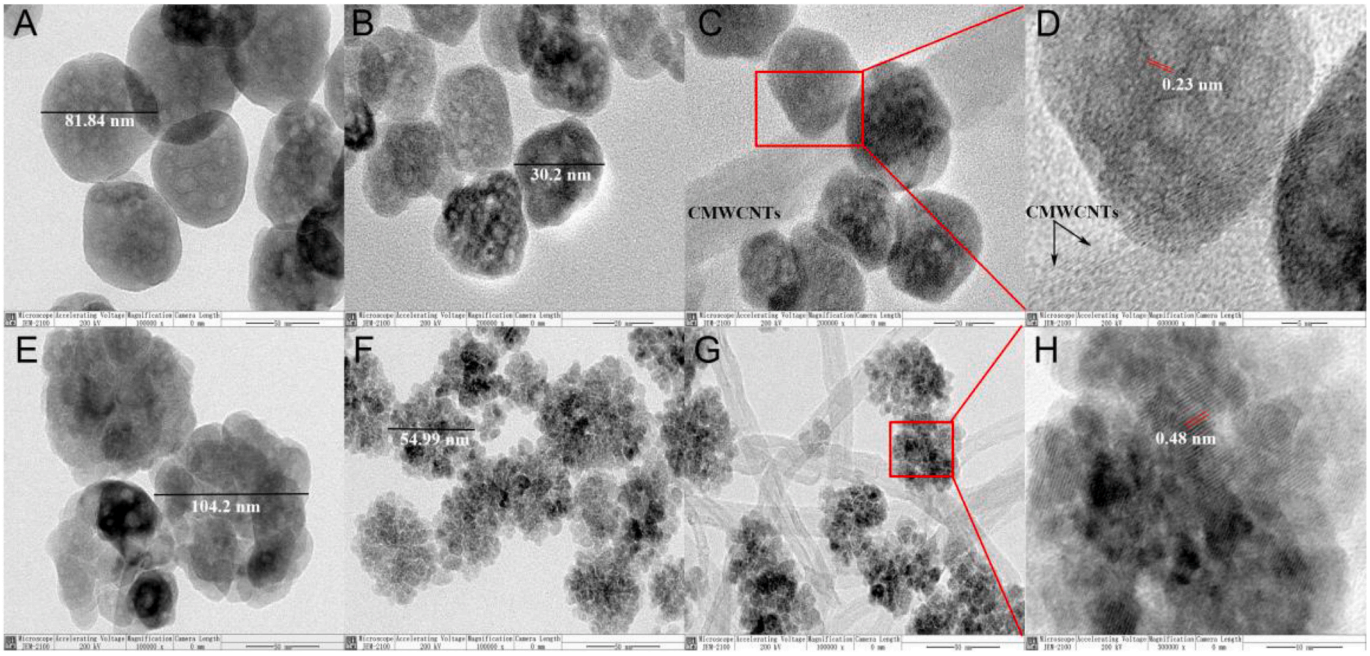


**Fig. 1.** TEM images of (A) $Fe_3O_4$, (B) $Fe_3O_4$-Pc, (C) $Fe_3O_4$-Pc-CMWCNTs, (E) $ZnFe_2O_4$, (F) $ZnFe_2O_4$-Pc, and (G) $ZnFe_2O_4$-Pc-CMWCNTs. The (D) and (H) show the enlarged view of (C) and (G).

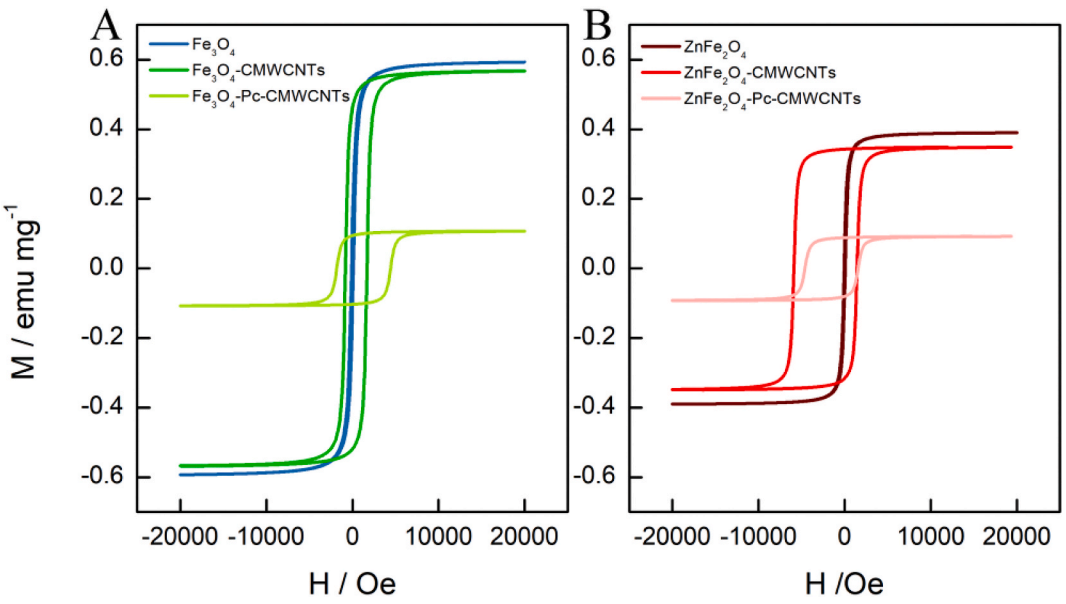


**Fig. 2.** VSM of different materials.

been influenced. As shown in Fig. S2, the construction of $Fe_3O_4$-Pc-CMWCNTs/MGCE also could be accomplished within 30s (as shown in Supporting video).

To confirm the phase transparency and formation of the nanosphere, XRD results were recorded in Fig. 3A. The sharp peaks at value of 30.1°, 35.46°, 43.08°, 53.5°, 57.02°, and 62.62° in all samples representing (220), (311), (400), (422), (511), and (440) lattice planes of ferrites, which were consistent with previous reports [24,41–43]. Curve c and f displayed a typical peak of CMWCNTs at around 24° (002), suggesting CMWCNTs were connected efficaciously on the nanosphere. Compared with $Fe_3O_4$ and $ZnFe_2O_4$, lower peak intensities could be observed in curve b, c, e, and f because the addition of carbon derivatives affected the crystallinity of hybrid nanomaterials, further suggesting the formation of a complex of ferrites, phthalocyanine, and CMWCNTs [44]. All the results demonstrated that the hybrid ferrites nanocomposites had been successfully synthesized.

Fig. 3B records the FT-IR spectra of $Fe_3O_4$, $ZnFe_2O_4$, $Fe_3O_4$-Pc-CMWCNTs, and $ZnFe_2O_4$-Pc-CMWCNTs. $Fe_3O_4$ and $ZnFe_2O_4$ had the stretching band appeared at 580 cm$^{-1}$, which was distributed to Fe–O stretching vibration. The clearly observed stretching bands at 841 cm$^{-1}$, 1010 cm$^{-1}$, and 1500 cm$^{-1}$ were attributed to the characteristic peaks of phthalocyanine, indicating a successful formation of phthalocyanine [40,45]. Besides, the weak peak appeared around 946 cm$^{-1}$ was the result of metal-ligand vibration, which referred to the formation of coordinate bonds between nitrogen and metal elements in the process of phthalocyanine formation [39,46]. Additionally, peaks located at 1463 cm$^{-1}$, 1580 cm$^{-1}$, and 1722 cm$^{-1}$ were assigned to the $CH_2$, CMWCNTs, and C═O, respectively, proving that the carboxyl group had been introduced in MWCNTs [47–49]. All the above evidences confirmed that the hybrid metal-phthalocyanine-sphere had been composed successful.

The electronic structure and valence state of the obtained nanomaterials were studied by XPS technology as shown in Fig. 4A. The C 1s, O 1s, Fe 2p, Zn $2p_{1/2}$ and Zn $2p_{3/2}$ regions at 282.3 eV, 529.1 eV, 710 eV, 1042.9 eV, and 1020.6 eV in the XPS spectra can be clearly observed, verifying the presence of C, O, Fe, and Zn elements in $Fe_3O_4$-Pc-CMWCNTs and $ZnFe_2O_4$-Pc-CMWCNTs, respectively. From the expanded XPS spectra of C 1s spectrum of $Fe_3O_4$-Pc-CMWCNTs and $ZnFe_2O_4$-Pc-CMWCNTs (Fig. 4B), there were five forms of C, namely C–C/C═C (284 eV), C–O/C–N (285 eV), and O–C═O (287 eV), confirming the doping of phthalocyanine and the carboxylation of MWCNTs. As illustrated in Fig. 4C, from Fe 2p spectrum, it is apparently observed two types of Fe, $Fe^{3+}$ (710.1 eV, 710.2 eV) and $Fe^{2+}$ (712.2 eV,

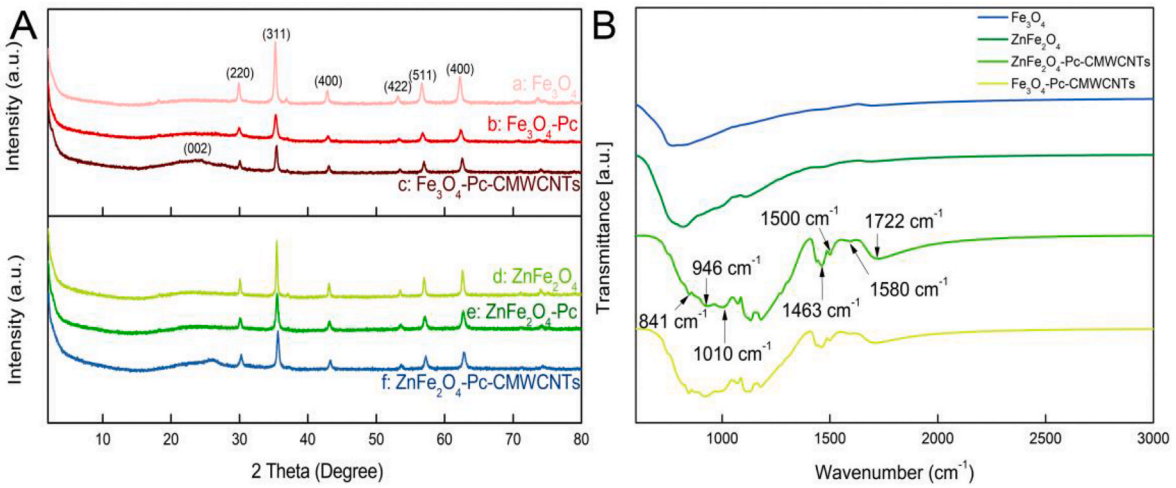


**Fig. 3.** (A) XRD spectra of stepwise-modified MGCE. (B) FTIR spectra of $Fe_3O_4$, $ZnFe_2O_4$, $Fe_3O_4$-Pc, and $ZnFe_2O_4$-Pc.

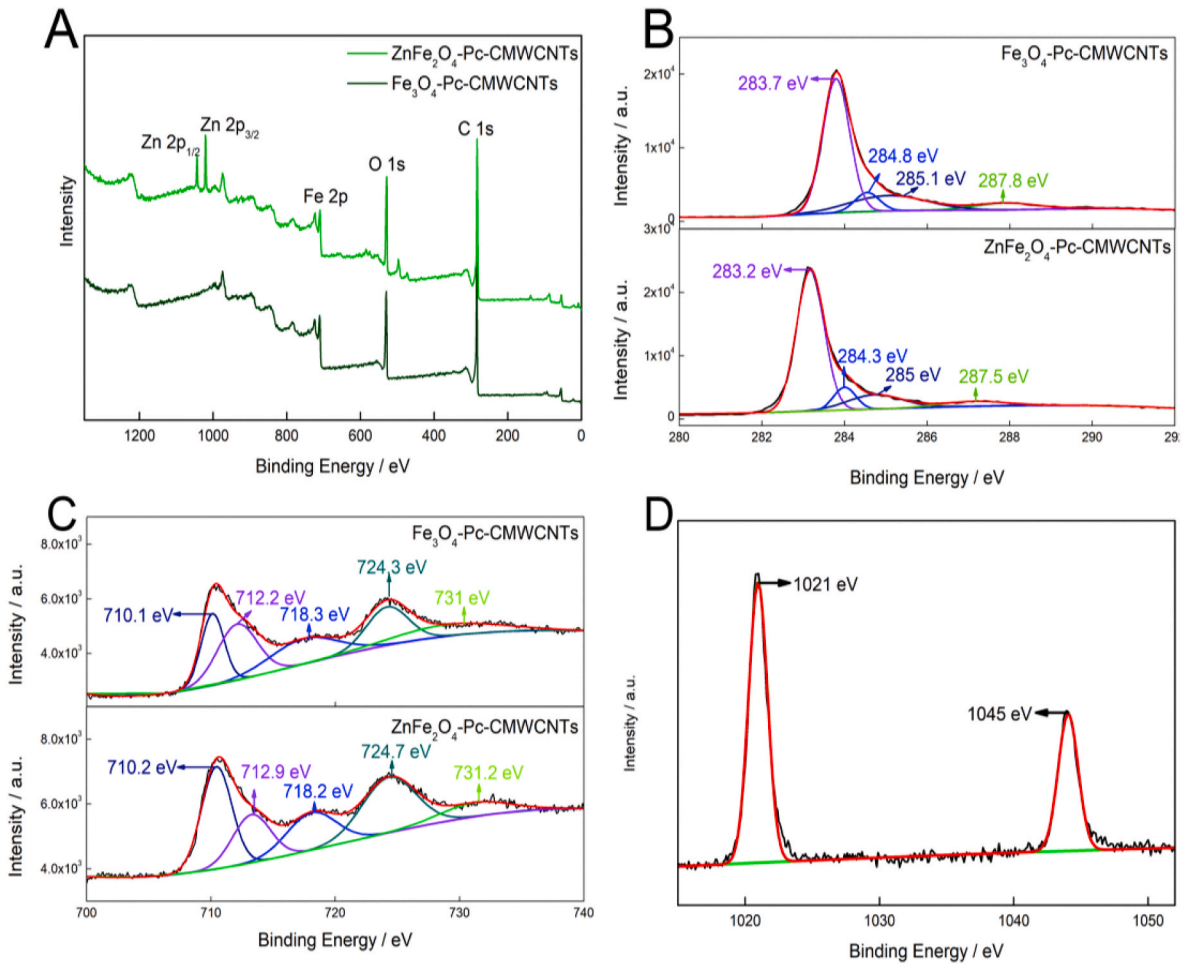


**Fig. 4.** (A) XPS full spectrum of $ZnFe_2O_4$-Pc-CMWCNTs and $Fe_3O_4$-Pc-CMWCNTs. (D) C 1s. (E) Fe 2p. (F) Zn.

712.9 eV) [50]. As for curve b, the deconvoluted of Fe $2p_{3/2}$ coincided with the tetrahedral and octahedral site of ferrites, verifying there was $Fe^{3+}$ in $ZnFe_2O_4$-Pc-CMWCNTs [51]. With the doped zinc, the level of $Fe^{2+}$ decreased while $Fe^{3+}$ increased, which was consistent with the previous report [52]. Moreover, the satellite peak of 1021 eV and 1045 eV were rationally attributed to Zn $2p_{1/2}$ and Zn $2p_{3/2}$ in Fig. 4D, proving the presence of $Zn^{2+}$ in the $ZnFe_2O_4$-Pc-CMWCNTs [53]. All the evidence indicated that $Fe^{2+}$, $Fe^{3+}$ and $Zn^{2+}$ were the metal ions in the metal-ligand complex to form the ferrites-Pc-CMWCNTs.

### 3.2. Electrochemical behavior of the prepared magnetic glassy carbon electrode

To investigate the surface properties of the stepwise-modified electrode, the 10 mM $[Fe(CN)_6]^{3-/4-}$ in 100 mM KCl aqueous solution has been used for cyclic voltammetry (CV) analysis at 50 mV/s. As shown in Fig. 5A and B, the symmetric redox pairs of $Fe^{2+/3+}$ and reversible controllable processes were presented in all samples. With the gradual modification of the CMWCNTs, $Fe_3O_4$, and Pc, the $\Delta Ep$ decreased while the peak current increased, implying that the $Fe_3O_4$-Pc-CMWCNTs and $ZnFe_2O_4$-Pc-CMWCNTs had the ability to enhance the electron transfer rate by improving the electrode conductivity. In addition, the electrode effective areas can be calculated by following Randles-Sevcik equation [54]:

$$i_p = 2.69 \times 10^5 n^{3/2} D^{1/2} C_0 v^{1/2} A_{eff} \quad (1)$$

where $i_p$, $n$, D, $C_0$ and $v$ represent the redox peak current (μA), number of transferred electrons (1), diffusion coefficient of ferricyanide solution ($6.70 \pm 0.02 \times 10^{-6}$ $cm^2$ $s^{-1}$), concentration of the probe molecule (mM) and scan rate (V $s^{-1}$), respectively. The calculated $A_{eff}$ ($cm^2$) of the different electrode increased in a sequence of bare MGCE (0.0880 $cm^2$) < $Fe_3O_4$/MGCE (0.1217 $cm^2$) < $Fe_3O_4$-CMWCNTs/MGCE (0.1484 $cm^2$) < $Fe_3O_4$-Pc-CMWCNTs/MGCE (0.1662 $cm^2$), and bare MGCE (0.0850 $cm^2$) < $ZnFe_2O_4$/MGCE (0.1115 $cm^2$) < $ZnFe_2O_4$-CMWCNTs/MGCE (0.1120 $cm^2$) < $ZnFe_2O_4$-Pc-CMWCNTs/MGCE (0.1589 $cm^2$). That means the hybrid metal-phthalocyanine- CMWCNTs nanocomposites significantly enhance the electrochemical surface area, which benefits the detection of rosmarinic acid. Notably, the value $A_{eff}$ of $Fe_3O_4$ was slightly higher than $ZnFe_2O_4$ (same as $Fe_3O_4$-CMWCNTs and $ZnFe_2O_4$-CMWCNTs; $Fe_3O_4$-Pc-CMWCNTs and $ZnFe_2O_4$-Pc-CMWCNTs), which probably due to the large lattices of $ZnFe_2O_4$ impeding the electron transfer of $Fe^{2+/3+}$.

Furthermore, electrochemical impedance measurements (EIS) was also applied to investigate the electronic conductivity of the samples and presented in Fig. 5C and D. It is noticeable that the resistance is sharply reduced along with the stepwise modification, indicating that the electron transfer ability of $Fe_3O_4$-Pc-CMWCNTs is promoted greatly compared with their counterparts. The EIS results also consist of the CV in $[Fe(CN)_6]^{3-/4-}$. This may result from the following reasons: (1) ferrites, as the thermodynamically stable metal oxide nanoparticles, have good conductivity and ferrimagnetic property to easily enhance the electron transfer between $Fe^{2+/3+}$ and the electrode; (2) CMWCNTs are carbon tubular structures with a large surface area, which also facilitate electron transfer between CMWCNTs and phthalocyanine via π–π stacking; (3) the 18 π-electron of phthalocyanine accelerates electron delocalization in hybrid ferrite-phthalocyanine-sphere, further

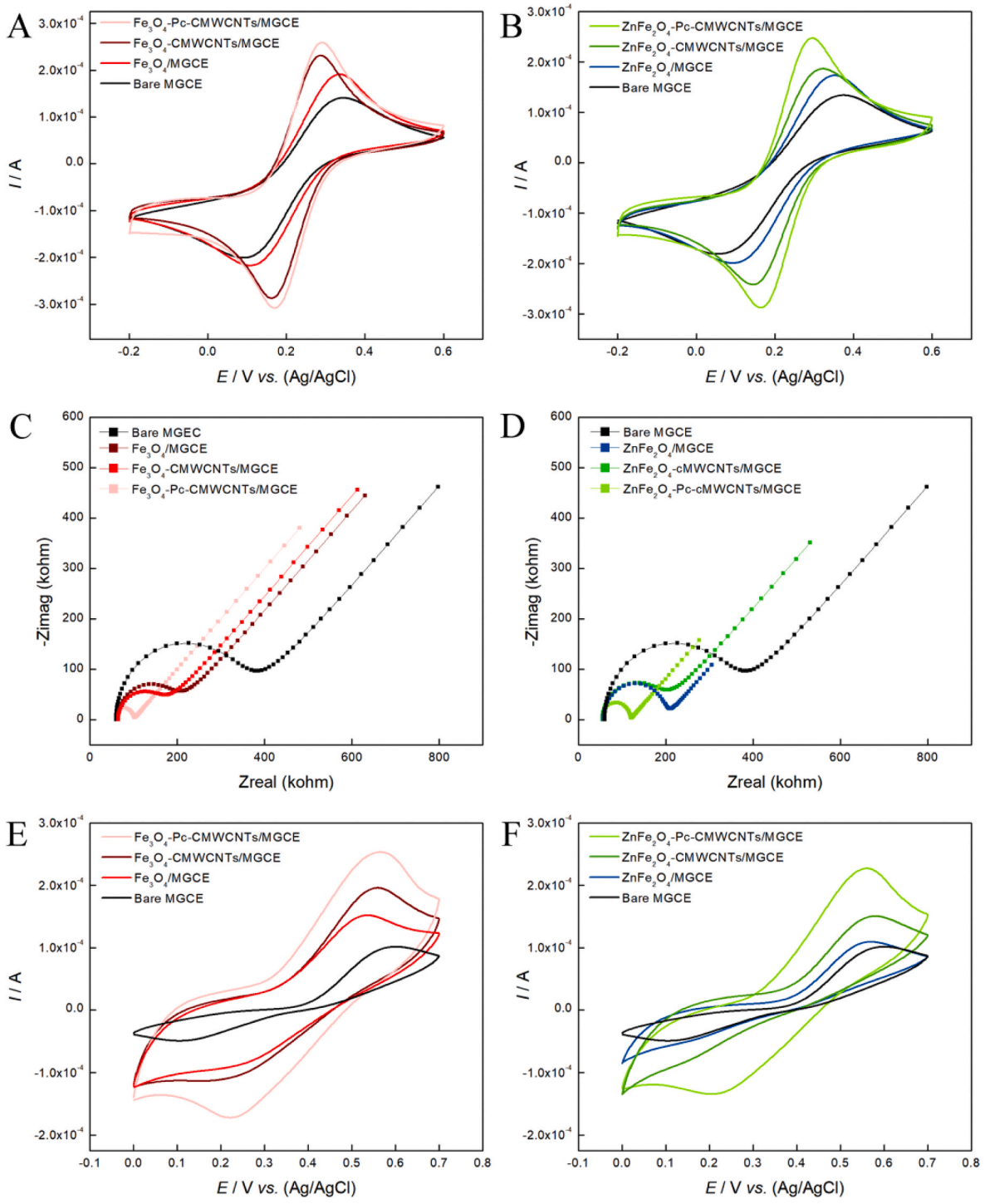


**Fig. 5.** (A, B) CV and (C, D) EIS response of $Fe_3O_4$, $Fe_3O_4$-Pc, $Fe_3O_4$-Pc-CMWCNTs, $ZnFe_2O_4$, $ZnFe_2O_4$-Pc, and $ZnFe_2O_4$-Pc-CMWCNTs in 5 mM $[Fe(CN)_6]^{3-/4-}$ solution containing 10 mM KCl. (E) and (F) show response of $Fe_3O_4$, $Fe_3O_4$-Pc, $Fe_3O_4$-Pc-CMWCNTs, $ZnFe_2O_4$, $ZnFe_2O_4$-Pc, and $ZnFe_2O_4$-Pc-CMWCNTs with1 mM RA in BR buffer.

improving the conductivity of the nanocomposites.

Fig. 5E and F depict CVs of 1 mM RA in BR buffer on different MGCEs. It is found that a pair of feeble redox peak current at 0.1 V and 0.593 V on the bare MGCE. After immediate adsorption of $Fe_3O_4$ nanoparticles, a higher *I*p appeared, illustrating $Fe_3O_4$ had a catalytical ability towards RA. After the addition of CMWCNTs and Pc, a directly higher current response had achieved 253.1 μA and 172.4 μA, which was 1.25, 1.66, and 2.5 times higher than $Fe_3O_4$-CMWCNTs/MGCE, $Fe_3O_4$/MGCE, and bare MGCE, respectively. The significant improvements of signals further confirmed that $Fe_3O_4$-Pc-CMWCNTs had the excellent activity of signal amplification and RA catalysis. In addition, the electrocatalytic behaviors of $ZnFe_2O_4$-Pc-CMWCNTs have been tested and reached similar conclusions. The *I*p of $ZnFe_2O_4$-Pc-CMWCNTs/MGCE was 1.51, 2.07, and 2.23 folds above $ZnFe_2O_4$-CMWCNTs/MGCE, $ZnFe_2O_4$/MGCE, and MGCE. It is noteworthy that the electrocatalytic capacity of $Fe_3O_4$-Pc-CMWCNTs is 1.1 times higher than $ZnFe_2O_4$-Pc-CMWCNTs, which could be contributed to the unique structure and properties of $Fe_3O_4$-Pc-CMWCNTs nanocomposites. Firstly, hybrid

ferrite acts as a nanocatalyst to foster the redox of RA, while the ferric ions located in octahedral sites are easier to connect the RA molecules on a smooth surface. Besides, $Fe_3O_4$-Pc-CMWCNTs have a shorter hopping length for the electronic transfer of ferric ions than $ZnFe_2O_4$-CMWCNTs. Compared with $Fe_3O_4$-Pc-CMWCNTs, zinc ferrite with a larger lattice hinders the electronic transfer of ferric ions. Therefore, the MGCE modified with $Fe_3O_4$-Pc-CMWCNTs nanocomposites displayed a more distinguished performance than the $ZnFe_2O_4$-CMWCNTs ones on the analysis of RA.

### 3.3. Optimization of experimental conditions

Optimal pH, and loading amounts of $Fe_3O_4$-Pc-CMWCNTs and $ZnFe_2O_4$-Pc-CMWCNTs were studied by CV containing 0.5 mM RA (Fig. S3). In this study, six parallel tests using different amounts of the obtained nanohybrids (20, 40, 60, 80, 100, and 120 μL) were completed with MGCE in each group. As shown in Fig. S3A and S3B insert, a plot of the RA oxidation peaks against the amount of the materials decorated on the MGCE undoubtedly exhibited the current reached a maximum at 80 μL and 100 μL for $Fe_3O_4$-Pc-CMWCNTs and $ZnFe_2O_4$-Pc-CMWCNTs, respectively.

The impacts of pH value on the redox currents of RA at $Fe_3O_4$-Pc-CMWCNTs/MGCE and $ZnFe_2O_4$-Pc-CMWCNTs/MGCE was also studied in the BR buffer solutions (pH = 2–8). In Fig. S3C and S3D, it can be observed that the peak current increased with the rising pH value from 2 to 5, while the currents expeditiously dropped over 5. The same results can be concluded from the inserts. Meanwhile, the anodic peak potential ($E_{pa}$) shifted negatively with the increased pH, implying the proton transfer occurred in the electrochemical process of RA. Thus, the peak current signal decreased beyond pH 5, presumably due to insufficient protons donation in RA oxidation process. Therefore, BR buffer with pH 5 was chosen as the optimal supporting electrolytes in the subsequent analysis. It can be found a linear relationship between $E_{pa}$ and pH on both $Fe_3O_4$-Pc-CMWCNTs/MGCE (Fig. S3E) and $ZnFe_2O_4$-Pc-CMWCNTs/MGCE (Fig. S3F). The linear regression equations were $y = -0.0555x + 0.7203$ (2) and $y = -0.052x + 0.6905$(3), respectively. The slopes of linear equation are closed to the theoretical value of −57.6 mV/pH, which means the number of proton and electron is equal in transfer reaction [55,56].

The behavior and the electrochemical property of RA redox on the electrode surface also have been studied by CVs at diverse scan rates (from 10 to 80 mv $s^{-1}$). As shown in Fig. S4A and S4C, the peak potential shifted towards positive direction along with the scan rate rising. At the same time, the signal was enhanced linearly proportional to the logarithm of scan rate owing to the interface capacitance charging in the process of charge transfer. The linear equations can be expressed as $Ip = 2.559E^{-5}\sqrt{V} + 1.5966E^{-5}$ (4) and $Ip = 1.8936E^{-5}\sqrt{V} + 7.1013E^{-5}$ (5) corresponding to $Fe_3O_4$-Pc-CMWCNTs/MGCE and $ZnFe_2O_4$-Pc-CMWCNTs/MGCE, respectively. The above results demonstrate that the electrochemical kinetics of RA are diffusion-limited processes on the modified electrode surface. With the aim of reducing interference influence, the 50 mv $s^{-1}$ was selected for the following tests.

### 3.4. The electrochemical mechanism of redox of RA with the proposed sensor

On the basis of the above results and the previous reports, the redox mechanism of RA was performed as shown in Fig. 6. In view of the equal number of protons and electrons in the transfer reaction, the strategy of RA redox is based on diffusion auxiliary electrocatalysis. Firstly, the RA diffuses from the aqueous solution towards the modified sensor surface and then adheres to the superficial hybrid sphere. Secondly, due to the alkyl chain of RA has the ability of electron-releasing, the electron density of the aromatic ring can be enhanced significantly, which makes the electron transfer of the redox process of RA more easily. Whereafter, along with the electron transport of $Fe^{3+}$-$Fe^{2+}$ ion pairs from hybrid ferrites, the redox process of RA has been further accelerated.

### 3.5. The quantitative performance of the proposed sensors

Differential pulse voltammetry was used for the quantitative detection of RA by the assembled sensor under the optimized conditions. As depicted in Fig. 7A and C, the initial response on $Fe_3O_4$-Pc-CMWCNTs/MGCE and $ZnFe_2O_4$-Pc-CMWCNTs/MGCE revealed at 0.2 μM and 2.85 μM, respectively. With the increased concentration of RA, the peak currents were respective linearly enhanced in two proper ranges, which indicating that the magnetic sensor is sensitive and sufficient for detection of RA in wide concentration range. The corresponding linear regression equations, detection range, and correlation coefficient were expressed as followed:

$Fe_3O_4$-Pc-CMWCNTs/MGCE:

$$I_{pa}(\mu A) = 0.1162C + 4.8300 \quad (6)$$

range from 0.2 μM to 24 μM, $R^2 = 0.9901$.

$$I_{pa}(\mu A) = 0.0217C + 7.1210 \quad (7)$$

range from 24 μM to 400 μM, $R^2 = 0.9914$.

$ZnFe_2O_4$-Pc-CMWCNTs/MGCE:

$$I_{pa}(\mu A) = 0.0400C + 1.9534 \quad (8)$$

range from 2.85 μM to 30 μM, $R^2 = 0.9930$.

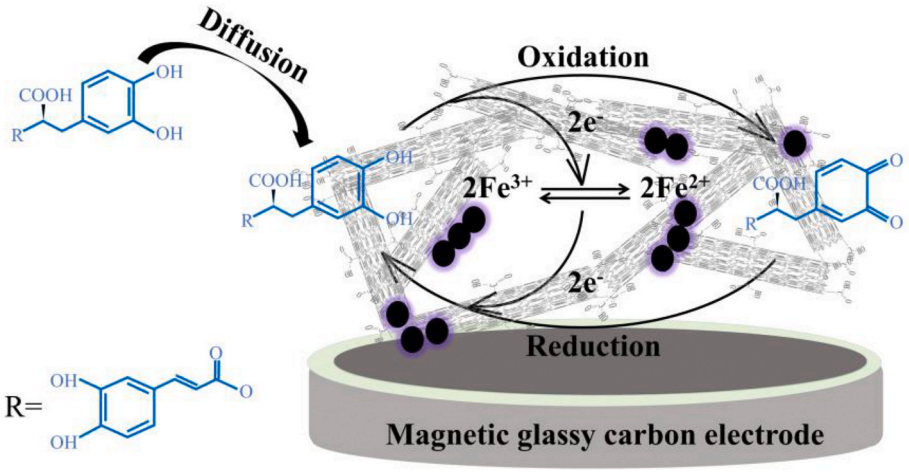


**Fig. 6.** The electrochemical mechanism of redox of RA.

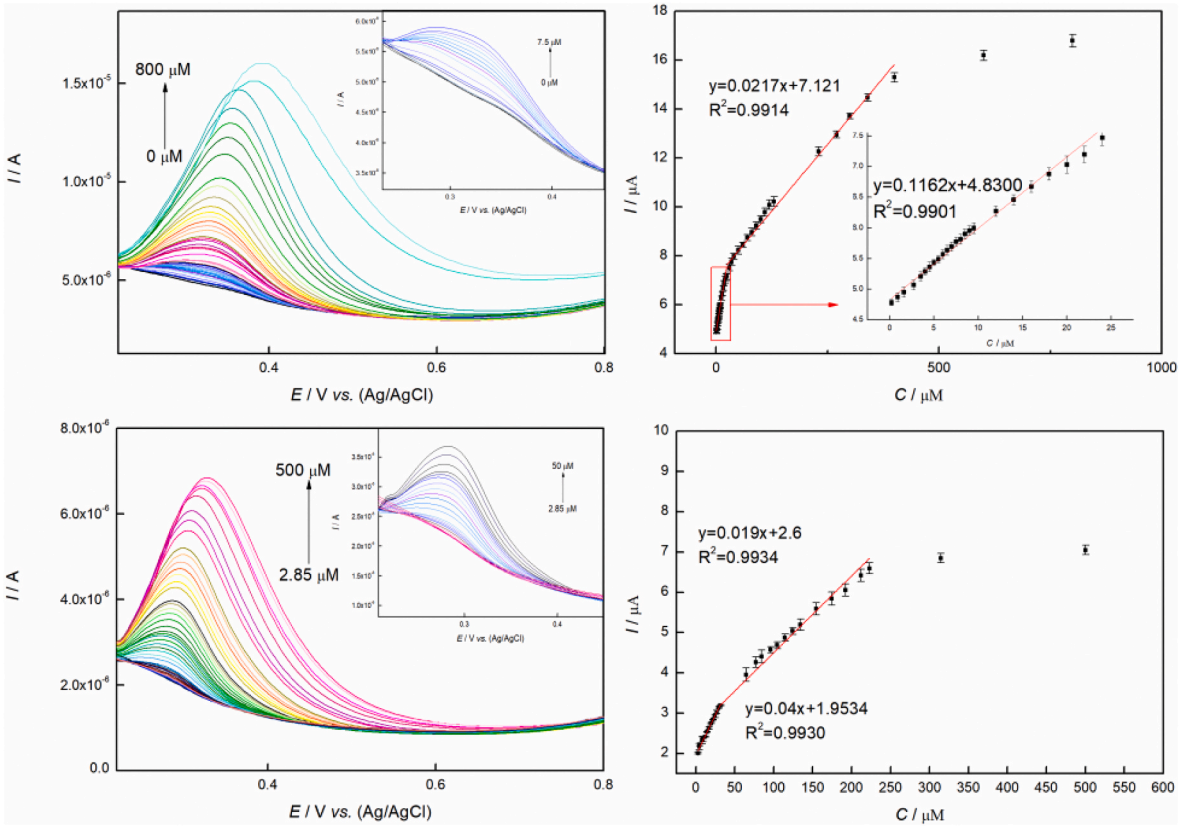


**Fig. 7.** (A) and (C) DPV responses of $Fe_3O_4$-Pc-CMWCNTs and $ZnFe_2O_4$-Pc-CMWCNTs with miscellaneous concentration of RA and the inserts exhibit close-up of the low normality of RA. (B) and (D) corresponding calibration with the concentration of RA.

$$I_{pa}(\mu A) = 0.0190C + 2.6000 \quad (9)$$

range from 30 μM to 223 μM, $R^2 = 0.9934$.

At a signal-to-noise factor ratio of 3, the limit of detections (LOD) of two sensors were approximated to 0.182 μM ($Fe_3O_4$-Pc-CMWCNTs/MGCE) and 0.6 μM ($ZnFe_2O_4$-Pc-CMWCNTs/MGCE). The limits of quantification (LOQ) were found as 0.6 μM of $Fe_3O_4$-Pc-CMWCNTs/MGCE and 2.02 μM of $ZnFe_2O_4$-Pc-CMWCNTs/MGCE at a signal-to-noise factor ratio of 10. Compared with the $ZnF_2O_4$-Pc-CMWCNTs/MGCE, the $Fe_3O_4$-Pc-CMWCNTs/MGCE had a widest linear range and lower LOD for sensitive detection of RA which was more efficiently for further application. The analytical performances of the present sensor were compared with the previously classical and electrochemical methods and they are presented in Table 1. $Fe_3O_4$-Pc-CMWCNTs/MGCE has a higher sensitivity and a wider linear range among the reported approaches, implying the prepared sensor is more suitable for the determination of RA.

### 3.6. The selectivity, reproducibility, repeatability and stability of the proposed sensors

To investigate the specificity of the obtained sensor based on $Fe_3O_4$-Pc-CMWCNTs, anti-interference tests have been performed by using different interferences (Fig. 8 A, B, and C). Solutions including 10-fold excess for common biologically interfering ions and coexisting vitamins were added with the presence of RA. After the injection of interferences, there was no significant change in the current response, indicating the sensing surface had a good selectivity. In addition, in the presence of equal concentration of RA analogs like chicoric acid, protocatechualdehyde, and puerarin, no noteworthy responses could be observed following the addition. New peak potentials appeared with the

**Table 1**
Different methods and electrochemical sensor for detection of RA.

| Methods | Electrode materials | linear range | Detection limit | Reference |
|---|---|---|---|---|
| ultra-fast liquid chromatography | C18 column packed with 2.6 μm particle size | 0.28–28 μM | 0.75 μM | [57] |
| UV–vis spectrophotometry | – | 1.4–56 μM | 1.064 μM | [12] |
| high-performance liquid chromatography with evaporative light scattering detection | Zorbax SB-C18 column | 48.16–481.6 μM | 18.76 μM | [58] |
| electrochemical sensor | Poly (*o*-Phenylenediamine)/Pt Nanoparticles | 1–55 μM | 0.5 μM | [59] |
| electrochemical sensor | laccase (1-n-butyl-3-methylimidazolium hexafluorophosphate and 1-n-butyl-3-methylimidazolium tetrafluoroborate) | 0.99–65.4 μM | 0.18 μM | [14] |
| electrochemical sensor | $Fe^{3+}Zn^{2+}$-[bis(2-pyridylmethyl) aminomethyl]-6-[(2-hydroxylbenzyl) (2-pyridyl-methyl) aminomethyl]-4-methyl-phenol | 29.8–38.3 μM | 2.3 μM | [60] |
| electrochemical sensor | laccase–nafion | 1–10 μM | 0.75 μM | [61] |
| electrochemical sensor | $Fe_3O_4$-Pc-cMWCNTs | 0.2–24 μM<br>24–400 μM | 0.182 μM | This work |

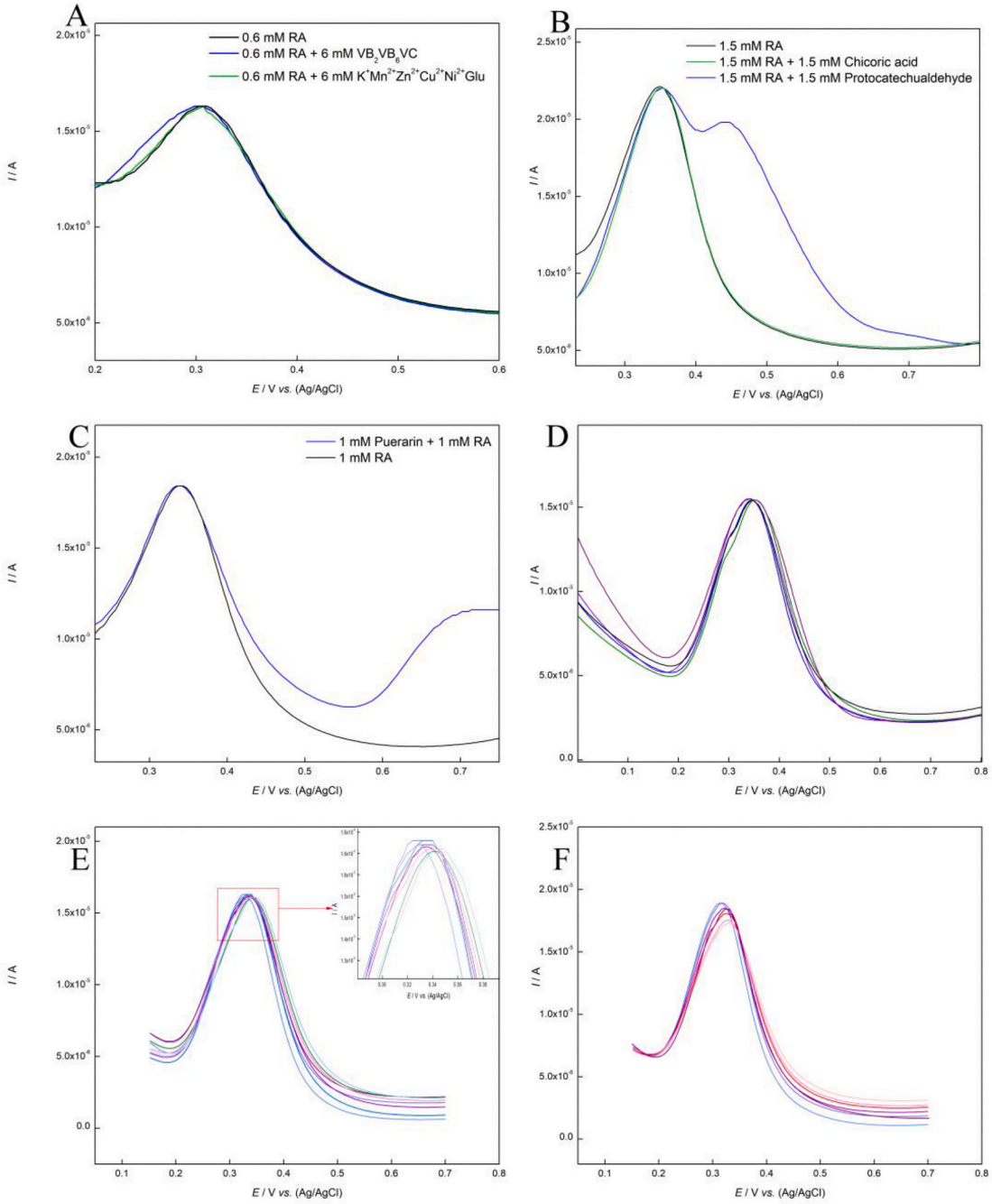


**Fig. 8.** (A), (B) and (C) DPV responses of $Fe_3O_4$-Pc-CMWCNTs with various interfering substances in presence of different concentrations of RA. (D) the reproducibility of $Fe_3O_4$-Pc-CMWCNTs/MGCE in 0.5 mM RA. (E) the repeatability of $Fe_3O_4$-Pc-CMWCNTs/MGCE in 0.5 mM RA. (F) DPV response of the same electrode in 0.6 mM RA with the interval of five days.

existence of protocatechualdehyde and puerarin, indicating the prepared sensor had not been affected and also could further apply in the exploration of multiple targets. Even though the potential of protocatechualdehyde is closing the oxidation potential of RA, the protocatechualdehyde cannot induce insignificant changes in the real test in our forecast because the content of protocatechualdehyde is a hundred times less than RA in plants [62]. The phenolic acid (caffeic acid, gallic acid, pyrocatechol, luteolin), and electroactive substances (adrenaline, dopamine, noradrenaline) were evaluated by $Fe_3O_4$-Pc-CMWCNTs/MGCE and no significant affect with the signal current response was detected (Fig. S5A and B). The above results all evidenced that our proposed sensor has an admirable selectivity for electrochemical detection of RA.

The reproducibility, repeatability, and long-term stability of $Fe_3O_4$-Pc-CMWCNTs/MGCE also have been verified in this work. As for the reproducibility, eight independent magnetic sensors were used for analysis in 0.5 mM RA solution, and the results were displayed in Fig. 8D. The relative standard deviation (RSD) value was 3.74%, suggesting that the $Fe_3O_4$-Pc-CMWCNTs/MGCE had a favorable reproducibility. In order to investigate the repeatability of the $Fe_3O_4$-Pc-CMWCNTs/MGCE, the RSD of oxidative peaks for five successive measurements by DPV on the same electrode was found to be 2.54% (Fig. 8E). After storage at 4 °C in the refrigerator for 30 days, the stability of the proposed sensor was also investigated with an interval of five days in 0.6 mM standard RA solution and shown in Fig. 8F. 91.6% of the initial current response was maintained after a month of storage,

indicating the outstanding long-term stability of the proposed sensor. All the evidences confirm that the fabricated biosensor has excellent selectivity, reproducibility, repeatability, and stability for electrochemical analysis of RA.

### 3.7. Application in real samples

To evaluate the effective adaptability in real samples, the standard addition method was used for analysing the practical performance of the constructed sensor in leach liquor of plants and human serum samples as shown in Table S1. The accurate amount of RA was added in real samples and tested by $Fe_3O_4$-Pc-CMWCNTs/MGCE and HPLC. Through calculating the obtained DPV value based on the equation in Fig. 7, the recoveries ranged within 98–103%. Besides, the HPLC results and the electrochemical results were compared using statistical method (*F* test and *t*-test), which shows no significant difference (P value $> 0.05$) between two method results. All results proved that the proposed RA sensor had excellent and accurate practicality and a potential to further applications in the quality control and study on drug metabolism.

## 4. Conclusion

In this work, we proposed a novel method for a one-step synthesis of magnetic nanohybrids consisted of metal and phthalocyanine. A convenient electrochemical sensor also had been fabricated by using a detachable magnetic electrode for sensitive and rapid analysis of RA in real samples. Utilizing CMWCNTs and Pc displayed extraordinarily improved active surface area and conductivity, which effectively amplified the electrochemical signal. Compared with $ZnFe_2O_4$-Pc-CMWCNTs based on prevalent ferrites, our $Fe_3O_4$-Pc-CMWCNTs exhibited more remarkably catalytic ability towards RA since their narrow lattices were conducive to accelerate the electron transfer of $Fe^{2+/3+}$. Owing to the excellent properties of $Fe_3O_4$-Pc-CMWCNTs, the sensor exhibited admirable performances for RA detection with a wide linear range from 0.2 to 400 μM and a low LOD of 0.182 μM, which was 3.29 times lower than its counterpart $ZnFe_2O_4$-Pc-CMWCNTs/MGCE. With excellent selectivity, reproducibility, repeatability, and stability, the proposed sensor has achieved the analysis of RA in plant samples and human serum samples, indicating it could be a promising candidate for quality control and investigation of drug metabolism in animals.

## Credit author statement

Zihua Wang: Conceptualization, Methodology, Investigation, Formal analysis, Writing – original draft, Visualization, Writing – review & editing; Yunyun Wang: Investigation, Formal analysis. Shengnan Yang: Investigation, Validation. Lan Xue: Investigation. Wei Feng: Writing – review & editing. Xinran Liu: Writing – review & editing. Binshuai Li: Writing – review & editing. Mengai Yin: Writing – review & editing. Jun Jiao: Writing – review & editing, Writing – original draft. Qiang Chen.: Supervision, Project administration, Funding acquisition, Writing – review & editing.

## Declaration of competing interest

The authors declare that they have no known competing financial interests or personal relationships that could have appeared to influence the work reported in this paper.

## Acknowledgments

This work was supported by the National Natural Science Foundation of China. (grant nos. 81671779, 81871451), and the Projects of Tianjin Science and Technology Support Program (No. S20YBL760).

## Appendix A. Supplementary data

Supplementary data to this article can be found online at https://doi.org/10.1016/j.talanta.2021.122165.

## References

[1] J. Moore, M. Megaly, A.J. MacNeil, P. Klentrou, E. Tsiani, Rosemary extract reduces Akt/mTOR/p70S6K activation and inhibits proliferation and survival of A549 human lung cancer cells, Biomed. Pharmacother. 83 (2016) 725–732.
[2] S. Anwar, A. Shamsi, M. Shahbaaz, A. Queen, P. Khan, G.M. Hasan, A. Islam, M. F. Alajmi, A. Hussain, F. Ahmad, M.I. Hassan, Rosmarinic acid exhibits anticancer effects via MARK4 inhibition, Sci. Rep. 10 (1) (2020) 10300.
[3] Y.L. Ngo, C.H. Lau, L.S. Chua, Review on rosmarinic acid extraction, fractionation and its anti-diabetic potential, Food Chem. Toxicol. 121 (2018) 687–700.
[4] S. Javidanpour, M. Dianat, M. Badavi, S.A. Mard, The cardioprotective effect of rosmarinic acid on acute myocardial infarction and genes involved in Ca2+ homeostasis, Free Radic. Res. 51 (11–12) (2017) 911–923.
[5] J. Han, D. Wang, L. Ye, P. Li, W. Hao, X. Chen, J. Ma, B. Wang, J. Shang, D. Li, Rosmarinic acid protects against inflammation and cardiomyocyte apoptosis during myocardial ischemia/reperfusion injury by activating peroxisome proliferator-activated receptor gamma, Front. Pharmacol. 8 (2017) 456.
[6] Z.-Q. Wang, Q.-Y. Song, J.-C. Su, W. Tang, J.-G. Song, X.-J. Huang, J.-m. An, Y.-L. Li, W.-C. Ye, Y. Wang, Caffeic acid oligomers from Mesona chinensis and their in Vitro antiviral activities, Fitoterapia (2020) 104603.
[7] E. Chigusa, T. Kiyotaka, U. Koji, Structure-activity Relations of Rosmarinic Acid Derivatives for the Amyloid β Aggregation Inhibition and Antioxidant Properties, 2017.
[8] A.G. Adomako-Bonsu, S.L. Chan, M. Pratten, J.R. Fry, Antioxidant activity of rosmarinic acid and its principal metabolites in chemical and cellular systems: importance of physico-chemical characteristics, Toxicol. Vitro 40 (2017) 248–255.
[9] B.-R. Jin, K.-S. Chung, S.-Y. Cheon, M. Lee, S. Hwang, S.N. Hwang, K.-J. Rhee, H. J, An, Rosmarinic acid suppresses colonic inflammation in dextran sulphate sodium (DSS)-induced mice via dual inhibition of NF-κB and STAT3 activation, Sci. Rep. 7 (2017) 46252.
[10] K. Jiang, X. Ma, S. Guo, T. Zhang, G. Zhao, H. Wu, X. Wang, G. Deng, Anti-inflammatory effects of rosmarinic acid in lipopolysaccharide-induced mastitis in mice, Inflammation 41 (2) (2018) 437–448.
[11] P. Li, A. Liu, Y. Li, B. Yuan, W. Xiao, Z. Liu, S. Zhang, H. Lin, Development and validation of an analytical method based on HPLC-ELSD for the simultaneous determination of rosmarinic acid, carnosol, carnosic acid, oleanolic acid and ursolic acid in rosemary, Molecules 24 (2) (2019) 323.
[12] F. Casanova, B.N. Estevinho, L. Santos, Preliminary studies of rosmarinic acid microencapsulation with chitosan and modified chitosan for topical delivery, Powder Technol. 297 (2016) 44–49.
[13] F.N. Fachel, M.C. Nemitz, B. Medeiros-Neves, K.S. Veras, V.L. Bassani, L.S. Koester, A.T. Henriques, H.F. Teixeira, A novel, simplified and stability-indicating high-throughput ultra-fast liquid chromatography method for the determination of rosmarinic acid in nanoemulsions, porcine skin and nasal mucosa, J. Chromatogr. B 1083 (2018) 233–241.
[14] A.C. Franzoi, J. Dupont, A. Spinelli, I.C. Vieira, Biosensor based on laccase and an ionic liquid for determination of rosmarinic acid in plant extracts, Talanta 77 (4) (2009) 1322–1327.
[15] S.A. Eremia, G.L. Radu, S.C. Litescu, Monitoring of rosmarinic acid accumulation in sage cell cultures using laccase biosensor, Phytochem. Anal. 24 (1) (2013) 53–58.
[16] K.V. Özdokur, Ç.C. Koçak, Simultaneous determination of rosmarinic acid and protocatechuic acid at poly (o-Phenylenediamine)/Pt nanoparticles modified glassy carbon electrode, Electroanalysis 31 (12) (2019) 2359–2367.
[17] M.L. Aparna, A.N. Grace, P. Sathyanarayanan, N.K. Sahu, A comparative study on the supercapacitive behaviour of solvothermally prepared metal ferrite (MFe2O4, M = Fe, Co, Ni, Mn, Cu, Zn) nanoassemblies, J. Alloys Compd. 745 (2018) 385–395.
[18] L.E. Smart, An Introduction to Crystal Structures, Solid State Chemistry, CRC Press2020, pp. 1-63.
[19] M. Amiri, K. Eskandari, M. Salavati-Niasari, Magnetically retrievable ferrite nanoparticles in the catalysis application, Adv. Colloid Interface Sci. 271 (2019) 101982.
[20] Q. Hu, Y. Shen, J.W. Chew, T. Ge, C.-H. Wang, Chemical looping gasification of biomass with Fe2O3/CaO as the oxygen carrier for hydrogen-enriched syngas production, Chem. Eng. J. 379 (2020) 122346.
[21] N. Doufar, M. Benamira, H. Lahmar, M. Trari, I. Avramova, M.T. Caldes, Structural and photochemical properties of Fe-doped ZrO2 and their application as photocatalysts with TiO2 for chromate reduction, J. Photochem. Photobiol. Chem. 386 (2020) 112105.
[22] T. Jiang, Y. Wang, Z. Li, H. Aslan, L. Sun, Y. Sun, W. Wang, M. Yu, Prussian blue-encapsulated Fe3O4 nanoparticles for reusable photothermal sterilization of water, J. Colloid Interface Sci. 540 (2019) 354–361.
[23] F. Qu, W. Shang, T. Thomas, S. Ruan, M. Yang, Self-template derived ZnFe2O4 double-shell microspheres for chemresistive gas sensing, Sensor. Actuator. B Chem. 265 (2018) 625–631.
[24] H. Karimi-Maleh, C.T. Fakude, N. Mabuba, G.M. Peleyeju, O.A. Arotiba, The determination of 2-phenylphenol in the presence of 4-chlorophenol using nano-Fe3O4/ionic liquid paste electrode as an electrochemical sensor, J. Colloid Interface Sci. 554 (2019) 603–610.

[25] W. Hu, D. Li, Y. Yang, T. Li, H. Chen, P. Liu, Copper ferrite supported gold nanoparticles as efficient and recyclable catalyst for liquid-phase ethanol oxidation, J. Catal. 357 (2018) 108–117.
[26] Y. Jin, J. Qian, K. Wang, X. Yang, X. Dong, B. Qiu, Fabrication of multifunctional magnetic FePc@ Fe3O4/reduced graphene oxide nanocomposites as biomimetic catalysts for organic peroxide sensing, J. Electroanal. Chem. 693 (2013) 79–85.
[27] A.K. Das, R. Kuchi, P.C. Van, Y. Sohn, J.-R. Jeong, Development of an Fe3O4@Cu silicate based sensing platform for the electrochemical sensing of dopamine, RSC Adv. 8 (54) (2018) 31037–31047.
[28] E. Ortí, J.L. Brédas, Electronic structure of metal-free phthalocyanine: a valence effective Hamiltonian theoretical study, J. Chem. Phys. 89 (2) (1988) 1009–1016.
[29] l.T. De, P. Vázquez, F. Agulló-López, T. Torres, Phthalocyanines and related compounds:organic targets for nonlinear optical applications, J. Mater. Chem. 8 (8) (1998) 1671–1683.
[30] H. Lyu, D. Yin, B. Zhu, G. Lu, Q.-Y. Liu, X. Zhang, X. Zhang, Metal-Free 2(3),9 (10),16(17),23(24)-octamethoxyphthalocyanine-modified uniform CoSn(OH)6 nanocubes: enhanced peroxidase-like activity, catalytic mechanism, and fast colorimetric sensing for cholesterol, ACS Sustain. Chem. Eng. 8 (25) (2020) 9404–9414.
[31] N.B. McKeown, Phthalocyanine Materials: Synthesis, Structure and Function, Cambridge University Press1998.
[32] J. Jiang, Functional phthalocyanine molecular materials, ACS Sens. 7 (2019) 1934–1941.
[33] Z. Zeng, X. Fang, W. Miao, Y. Liu, T. Maiyalagan, S. Mao, Electrochemically sensing of trichloroacetic acid with iron (II) phthalocyanine and Zn-based metal organic framework nanocomposites, ACS Sens. 4 (7) (2019) 1934–1941.
[34] N. Diab, D.M. Morales, C. Andronescu, M. Masoud, W. Schuhmann, A sensitive and selective graphene/cobalt tetrasulfonated phthalocyanine sensor for detection of dopamine, Sensor. Actuator. B Chem. 285 (2019) 17–23.
[35] N.P. Shetti, D.S. Nayak, S.J. Malode, R.R. Kakarla, S.S. Shukla, T.M. Aminabhavi, Sensors based on ruthenium-doped TiO2 nanoparticles loaded into multi-walled carbon nanotubes for the detection of flufenamic acid and mefenamic acid, Anal. Chim. Acta 1051 (2019) 58–72.
[36] R. Gupta, B. Singh, Chemical modification of carboxylated MWCNTs for enhanced electrical conducting and magnetic properties, Mater. Sci. Eng., B 262 (2020) 114730.
[37] F. Hu, W. Zhang, W. Meng, Y. Ma, X. Zhang, Y. Xu, P. Wang, Y. Gu, Ferrocene-labeled and purification-free electrochemical biosensor based on ligase chain reaction for ultrasensitive single nucleotide polymorphism detection, Anal. Chim. Acta 113 (10) (2020) 8152–8191.
[38] A.B. Sorokin, Phthalocyanine metal complexes in catalysis, Chem. Rev. 113 (10) (2013) 8152–8191.
[39] F. Meng, R. Zhao, Y. Zhan, Y. Lei, J. Zhong, X. Liu, One-step synthesis of Fe-phthalocyanine/Fe3O4 hybrid microspheres, Mater. Lett. 65 (2) (2011) 264–267.
[40] Z. Pu, X. Zhou, X. Yang, K. Jia, X. Liu, One step grafting of iron phthalocyanine containing flexible chains on Fe3O4 nanoparticles towards high performance polymer magnetic composites, J. Magn. Magn Mater. 385 (2015) 368–376.
[41] S. Venkateswarlu, B.N. Kumar, B. Prathima, Y. SubbaRao, N.V.V. Jyothi, A novel green synthesis of Fe3O4 magnetic nanorods using Punica Granatum rind extract and its application for removal of Pb(II) from aqueous environment, Arabian Journal of Chemistry 12 (4) (2019) 588–596.
[42] A. Habibi-Yangjeh, M. Mousavi, K. Nakata, Boosting visible-light photocatalytic performance of g-C3N4/Fe3O4 anchored with CoMoO4 nanoparticles: novel magnetically recoverable photocatalysts, J. Photochem. Photobiol. Chem. 368 (2019) 120–136.
[43] P. Guo, L. Cui, Y. Wang, M. Lv, B. Wang, X.S. Zhao, Facile synthesis of ZnFe2O4 nanoparticles with tunable magnetic and sensing properties, Langmuir 29 (28) (2013) 8997–9003.
[44] Y. Jin, J. Qian, K. Wang, X. Yang, X. Dong, B. Qiu, Fabrication of multifunctional magnetic FePc@Fe3O4/reduced graphene oxide nanocomposites as biomimetic catalysts for organic peroxide sensing, J. Electroanal. Chem. 693 (2013) 79–85.
[45] M. Socol, N. Preda, O. Rasoga, C. Breazu, I. Stavarache, F. Stanculescu, G. Socol, F. Gherendi, V. Grumezescu, G. Popescu-Pelin, M. Girtan, N. Stefan, Flexible heterostructures based on metal phthalocyanines thin films obtained by MAPLE, Appl. Surf. Sci. 374 (2016) 403–410.
[46] K. Nakamoto, Infrared and R Aman Spectra of Inorganic and Coordination Compounds, Handbook of Vibrational Spectroscopy, 2006.
[47] Y. Gao, Q. Li, Y. Shi, R. Cha, Preparation and application of cationic modified cellulose fibrils as a papermaking additive, International Journal of Polymer Science 2016 (2016) 6978434.
[48] H. Sadegh, G.A.M. Ali, A.S.H. Makhlouf, K.F. Chong, N.S. Alharbi, S. Agarwal, V. K. Gupta, MWCNTs-Fe3O4 nanocomposite for Hg(II) high adsorption efficiency, J. Mol. Liq. 258 (2018) 345–353.
[49] B. Bian, Q. Liu, S. Yu, Peroxidase mimetic activity of porphyrin modified ZnFe2O4/reduced graphene oxide and its application for colorimetric detection of H2O2 and glutathione, Colloids Surf. B Biointerfaces 181 (2019) 567–575.
[50] D. Wilson, M.A. Langell, XPS analysis of oleylamine/oleic acid capped Fe3O4 nanoparticles as a function of temperature, Appl. Surf. Sci. 303 (2014) 6–13.
[51] R. Shu, G. Zhang, X. Wang, X. Gao, M. Wang, Y. Gan, J. Shi, J. He, Fabrication of 3D net-like MWCNTs/ZnFe2O4 hybrid composites as high-performance electromagnetic wave absorbers, Chem. Eng. J. 337 (2018) 242–255.
[52] X. Li, E. Liu, Z. Zhang, Z. Xu, F. Xu, Solvothermal synthesis, characterization and magnetic properties of nearly superparamagnetic Zn-doped Fe3O4 nanoparticles, J. Mater. Sci. Mater. Electron. 30 (4) (2019) 3177–3185.
[53] A.A. Tahir, K.G.U. Wijayantha, Photoelectrochemical water splitting at nanostructured ZnFe2O4 electrodes, J. Photochem. Photobiol. Chem. 216 (2) (2010) 119–125.
[54] A.J. Bard, L.R. Faulkner, Electrochemical methods: fundamentals and applications, J. Chem. Educ. 60 (1980).
[55] M.R. de Rooij Dr, Electrochemical methods: fundamentals and applications, Anti-corrosion Methods & Mater. 50 (5) (2003).
[56] X. Yan, Y. Gu, C. Li, L. Tang, B. Zheng, Y. Li, Z. Zhang, M. Yang, Synergetic catalysis based on the proline tailed metalloporphyrin with graphene sheet as efficient mimetic enzyme for ultrasensitive electrochemical detection of dopamine, Biosens. Bioelectron. 77 (2016) 1032–1038.
[57] F.N.S. Fachel, M.C. Nemitz, B. Medeiros-Neves, K.S. Veras, V.L. Bassani, L. S. Koester, A.T. Henriques, H.F. Teixeira, A novel, simplified and stability-indicating high-throughput ultra-fast liquid chromatography method for the determination of rosmarinic acid in nanoemulsions, porcine skin and nasal mucosa, J. Chromatogr. B 1083 (2018) 233–241.
[58] P. Li, A. Liu, Y. Li, B. Yuan, W. Xiao, Z. Liu, S. Zhang, H. Lin, Development and validation of an analytical method based on HPLC-ELSD for the simultaneous determination of rosmarinic acid, Carnosol, Carnosic Acid, Oleanolic Acid and Ursolic Acid in Rosemary, Molecules 24 (2) (2019).
[59] K.V. Özdokur, Ç.C. Koçak, Simultaneous determination of rosmarinic acid and protocatechuic acid at poly(o-phenylenediamine)/Pt nanoparticles modified glassy carbon electrode, Electroanalysis 31 (12) (2019) 2359–2367.
[60] M. Santhiago, R.A. Peralta, A. Neves, G.A. Micke, I.C. Vieira, Rosmarinic acid determination using biomimetic sensor based on purple acid phosphatase mimetic, Anal. Chim. Acta 613 (1) (2008) 91–97.
[61] S.A.V. Eremia, G.-L. Radu, S.-C. Litescu, Monitoring of rosmarinic acid accumulation in sage cell cultures using laccase biosensor, Phytochem. Anal. 24 (1) (2013) 53–58.
[62] J.-P. Yuan, H. Chen, F. Chen, Simultaneous determination of rosmarinic acid, lithospermic acid B, and related phenolics in salvia miltiorrhiza by HPLC, Journal of Agricultural and Food Chemistry - J AGR FOOD CHEM 46 (1998).